SCIEPublish

Article

Exploring $Bi_4V_2O_{11}$ as Photoanode for Water Splitting with a Wide Range of Solar Light Capture and Suitable Band Potential

Xin Zhao [1,2], Ningsi Zhang [3], Yang Yu [4], Tao Fang [3], Jun Hu [5,*], Jianyong Feng [3,*] and Zhong Chen [1,*]

[1] School of Materials Science and Engineering, Nanyang Technological University, 50 Nanyang Avenue, Singapore 639798, Singapore; zhxin-8@outlook.com (X.Z.)
[2] College of Resources and Environmental Sciences, China Agricultural University, Beijing 100193, China
[3] Eco-materials and Renewable Energy Research Center (ERERC), College of Engineering and Applied Science, Nanjing University, Nanjing 210093, China; tpnju0504@163.com (N.Z.); vsfangtao@126.com (T.F.)
[4] Energy Foundation China, No. 19 Jianguomenwai Dajie, Beijing 100004, China; Yuyangalfaro@gmail.com (Y.Y.)
[5] School of Chemical Engineering, Northwest University, Xi'an 710069, China

* Corresponding author. E-mail: hujun@nwu.edu.cn (J.H.); fengjianyong@nju.edu.cn (J.F.); ASZChen@ntu.edu.sg (Z.C.)

Received: 21 February 2024; Accepted: 3 April 2024; Available online: 11 April 2024

ABSTRACT: $Bi_4V_2O_{11}$ possesses a bandgap of ~1.9 eV, and the band positions of minimum conduction band and maximum valence band straddle the redox potentials of H^+/H_2 and O_2/H_2O. In the current work, photoanode made of particulate $Bi_4V_2O_{11}$ film displays a wide range of light adsorption. However, when the anode was fabricated by drop-casting and examined for photoelectrochemical water splitting, the photocurrent density of the pristine $Bi_4V_2O_{11}$ was low. Improvement has then been carried out by Mo-doping. The Mo-doped $Bi_4V_2O_{11}$ photoanode achieves a maximum photocurrent density of 0.3 mA/cm^2 after a post deposition necking treatment to improve the connectivity of the drop-cast particles in the film. This material also shows a stability with maintaining 80% photocurrent after 2 h test. Discussion has been made on the displayed performance in PEC water splitting of the $Bi_4V_2O_{11}$ materials. Potential solutions have been proposed for this type of promising photoanode material for water splitting.

Keywords: Visible light photocatalyst; $Bi_4V_2O_{11}$; Photoelectrochemical water splitting; Photoanode

1. Introduction

Photoelectrochemical (PEC) splitting of water into hydrogen and oxygen is a promising route to produce clean and renewable H_2 energy [1–3]. Compared with the efficient p-type photocathodes, the low efficiency in oxygen evolution poses a great challenge on water splitting [4]. Recently, (oxy)nitride materials such as Ta_3N_5 [5–7], $LaTiO_2N$ [8,9], and $SrTaO_2N$ [10], $BaTaO_2N$ [11] have attracted a great deal of interest due to their high theoretical solar-to-hydrogen efficiency (over 15%), as well as suitable conduction and valence band positions for water splitting. However, most n-type non-oxide semiconductors are chemically unstable and easily oxidized by photo-generated holes [12]. Compared with the oxynitride materials, metal oxides are more promising to be stable photoanodes. Unfortunately, most of the currently reported metal oxides cannot harvest enough visible light due to their wide bandgaps, such as TiO_2, WO_3 and $BiVO_4$ [12–15]. Although hematite (α-Fe_2O_3) is a narrow band gap oxide photoanode material with bandgap around 2.0 eV, the bottoms of the conduction band of hematite is more positive (around 0.5 eV) than the water reduction potential. This would require a large external bias to overcome the potential difference [16]. Besides, very short hole diffusion length (only a few nano meters) and short carrier life time also limit the performance of hematite [17]. Thus, it is highly desirable to develop new visible-light driven materials that have proper band potential positions and could simultaneously harvest a wide range of visible light. $Bi_4V_2O_{11}$ has emerged as a visible light responsive photocatalyst and demonstrated ability for dye or organic waste degradation [18–24]. The visible light driven oxygen evolution performance was investigated by Jiang et al. [18] Santos et al. employed a low temperature phase as a hole inversion layer at the $BiVO_4/Bi_4V_2O_{11}$ interface [25,26]. Photocatalytic CO_2 reduction was also investigated utilizing Bi-quantum-dot-decorated $Bi_4V_2O_{11}$ hollow nanocakes [27]. Although electronic structure of orthorhombic $Bi_4V_2O_{11}$ has been investigated by density functional theory (DFT) to

https://doi.org/10.35534/prp.2024.10002

predict its possibility of photoelectrochemical water splitting [28], the material has not been thoroughly investigated as a photoelectrode for PEC water splitting. Furthermore, the doping effect has not been explored to enhance the PEC performance. Doping is a proven method for increasing carrier density, which consequently enhances the charge separation of the photocatalyst [29]. The efficacy of Mo doping in enhancing the $BiVO_4$ photocatalyst has been demonstrated [30]. This strategy, which has shown promise in $BiVO_4$, may similarly benefit $Bi_4V_2O_{11}$.

In the present study, the properties of $Bi_4V_2O_{11}$ photoanodes were investigated. $Bi_4V_2O_{11}$ powders, with and without Mo-doping, were prepared by solid state reaction. The photocurrent density and stability under PEC test condition have been investigated. The Mo-doped $Bi_4V_2O_{11}$ photoanode achieves a maximum photocurrent density of 0.3 mA/cm^2 after a post deposition treatment to improve the connectivity of the drop-cast particles in the film. $Bi_4V_2O_{11}$ displays a promising potential as a photoanode material for non-biased water splitting.

2. Experiment

2.1. Preparation of Pure and Mo Doped $Bi_4V_2O_{11}$ Powder Photocatalyst

Pristine $Bi_4V_2O_{11}$ particles were prepared by a solid-state reaction. Stoichiometric amount of Bi_2O_3, NH_4VO_3 were mixed and ground in an agate mortar with addition of a small amount of ethanol. The mixture was then sintered at 600 °C for 3 h and 800 °C for 10 h. The obtained red powder has some impurity phase which was ground again in an agate mortar, then sintered at 800 °C for 10 h for the second time to obtain a pure phase of $Bi_4V_2O_{11}$. Pure $Bi_4V_2O_{11}$ particles were obtained after grinding. Mo doped $Bi_4V_2O_{11}$ particles were synthesized by the same method, except adding suitable amount of MoO_3. The doping concentration is 3% according to the optimized Mo doping level in $BiVO_4$ reported by Luo et al. [13].

2.2. Fabrication of Particulate Films

Photoanode films were fabricated by drop casting method followed by necking treatment according to a method reported before [31]. Powder suspension was obtained by dispersing 20 mg powder into 500 μL isopropanol with sonication. The film was fabricated by dropping 50 μL suspension onto an FTO glass substrate (2 cm × 1 cm). After drying, another drop-casting process was conducted to obtain the film. The necking procedure was conducted by dropping 20 μL of ammonium metatungstate methanol solution (10 mM) on the dried film. This procedure was repeated for six times to improve the connectivity among the synthesized particles in the film. After that, half of the film was scrubbed to expose conductive substrate, then followed by heating at 500 °C for 1 h in air.

2.3. Pt Loading on the Powder Surface

1 wt% Pt was loaded as the co-catalyst by photoreduction using H_2PtCl_6. Typically, 0.1 g of photocatalyst, 100 mL of distilled water, 20 mL of CH_3OH, and 1% amount of $H_2PtCl_6{\cdot}6H_2O$ were placed in a glass vessel. The reactant solution was irradiated with a 300-W Xe lamp for 8 h with constant stirring. Then the Pt-loaded photocatalyst powder was filtered and washed thoroughly with deionized water and alcohol, subsequently dried at 60 °C for 12 h.

2.4. Water Splitting Test

The photocatalytic H_2 evolution reaction of powder samples was carried out in a Pyrex reaction vessel which was equipped into a closed gas circulation and evacuation system. The reaction was conducted in an aqueous solution containing 0.1 g of the 1 wt% Pt loaded $Bi_4V_2O_{11}$ catalyst. Methanol (20% *v*/*v*, 100 mL) was used as the sacrificial reagent. The reaction was performed under irradiation of a 300-W Xe lamp with the light intensity of 100 mW/cm^2. The evolved gas was then extracted and analysed by gas chromatography.

Photoelectrochemical measurements were conducted utilizing a three-electrode setup comprising a PCI4/300™ potentiostat controlled by PHE200™ software from Gamry Electronic Instruments, Inc. The configuration included a $Bi_4V_2O_{11}$ working electrode, a Pt foil serving as the counter electrode, and a reference electrode consisting of Ag/AgCl. A solar simulator (HAL-320, Asahi Spectra Co., Ltd., Tokyo, Japan) with an intensity of 100 mW·cm^{-2}, calibrated using a solar reference cell, was employed as the light source for the photoelectrochemical measurements. Photocurrent density testing employs a mask with an open area of 0.28 cm^2 positioned at the center. This configuration ensures greater uniformity in the film at the center to evaluate the real performance of the photoelectrode. Photocurrents associated with water oxidation were recorded in a 0.5 M Na_2SO_4 aqueous solution at a scan rate of 30 mV·s^{-1}. Additionally, photocurrents were measured under hole scavenger conditions to achieve approximately 100% charge transfer efficiency, in a solution comprised of 0.5 M Na_2SO_4 mixed with 0.1 M Na_2SO_3.

2.5. Characterization

The morphologies were examined via field emission scanning electron microscopy (FESEM, JEOL JSM-7600F, JEOL, Ltd., Tokyo, Japan). Crystallinity was determined through X-ray diffraction (XRD) analysis using a Shimadzu 6000 X-ray diffractometer equipped with Cu Kα radiation (λ = 0.154 nm), employing a 2θ scan mode with a fixed incidence angle of 1°. Light absorption characteristics were assessed by measuring reflectance and transmittance using a UV-visible spectrophotometer equipped with an integrating sphere (Lambda 750S, Perkin-Elmer, Shelton, CT, USA).

3. Results and Discussion

DFT calculation shows that α-$Bi_4V_2O_{11}$ possesses a monoclinic structure with a bandgap of 2.03 eV (Figure 1a). The valence band maximum is mainly composed of the O 2p orbital, and the conduction band minimum is composed of the O 2p and V 3d states. Figure 1b shows the band structure of α-$Bi_4V_2O_{11}$, which indicates that α-$Bi_4V_2O_{11}$ is an indirect bandgap semiconductor.

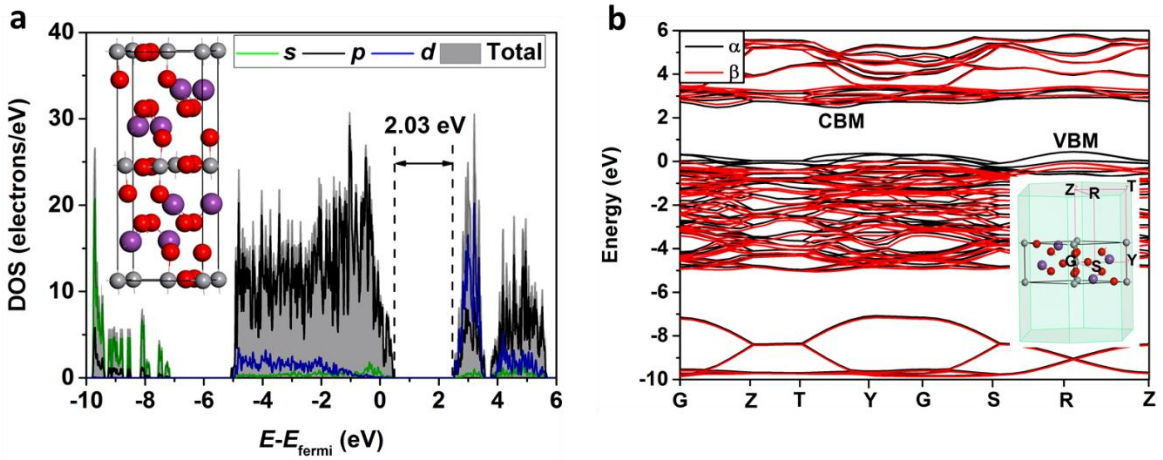

Figure 1. (**a**) Calculated local partial density of states and (**b**) band structure of α-$Bi_4V_2O_{11}$. Red, grey, and purple spheres in (**a**) represent O, V, and Bi atoms, respectively.

X-ray diffraction spectra of $Bi_4V_2O_{11}$ powder prepared by solid state reaction indicate they belong to α-$Bi_4V_2O_{11}$ (Powder Diffraction File No. 82-1481) without any detectable impurity (Figure 2a). Scanning electron microscopy (SEM) images of the $Bi_4V_2O_{11}$ samples also suggest well crystallized particles with smooth surface (Figure S1). The particle size of the $Bi_4V_2O_{11}$ samples is about several microns. Figure 2b shows that the as-synthesized red-coloured $Bi_4V_2O_{11}$ powders exhibit visible light absorption with optical absorption edges of about 600 nm. The Tauc plot $Bi_4V_2O_{11}$ (Figure 2c) is shown in Figure 1b. Using indirect bandgap model, calculation based on the Tauc plot suggests that $Bi_4V_2O_{11}$ possesses a bandgap of about 1.87 eV, which is consistent with the calculated results. Such a small bandgap corresponds to a theoretical solar to hydrogen efficiency of 21.6% and a maximum solar photocurrent of ~17.6 mA/cm^2 with a great potential for water splitting (Figure 2d).

$Bi_4V_2O_{11}$ film was fabricated by drop casting according to the reported method [31]. The film thickness was estimated to be a few microns according to the particle size (Figure S1). Mott-Schottky plot (Figure 3a) indicates the flat-band potential (V_F) of $Bi_4V_2O_{11}$ is −0.31 V vs. RHE. The flat-band potential represents the position of the Fermi level of the semiconductor and is generally considered to be located just under the conduction band of n-type semiconductors [32]. Hence, flat-band potential can be seen as the conduction band minimum level (CBM). Combining the bandgap value of 1.87 eV, we obtain the band position diagram of $Bi_4V_2O_{11}$ as shown in Figure 3b. The energy levels of CBM and valence band maximum (VBM) straddle the redox potentials of H^+/H_2 and O_2/H_2O, which makes the material suitable for water splitting. Figure 3c shows the photocatalytic H_2 evolution from a 20% (*v*/*v*) methanol aqueous solution (100 mL) over 1wt% Pt-loaded $Bi_4V_2O_{11}$ powder sample (100 mg) under irradiation. Under irradiation, H_2 was produced onto the surface of Pt-loaded $Bi_4V_2O_{11}$, indicating the activity of $Bi_4V_2O_{11}$ catalyst for H_2 evolution. This confirms that CBM of $Bi_4V_2O_{11}$ is negative than the water reduction potential.

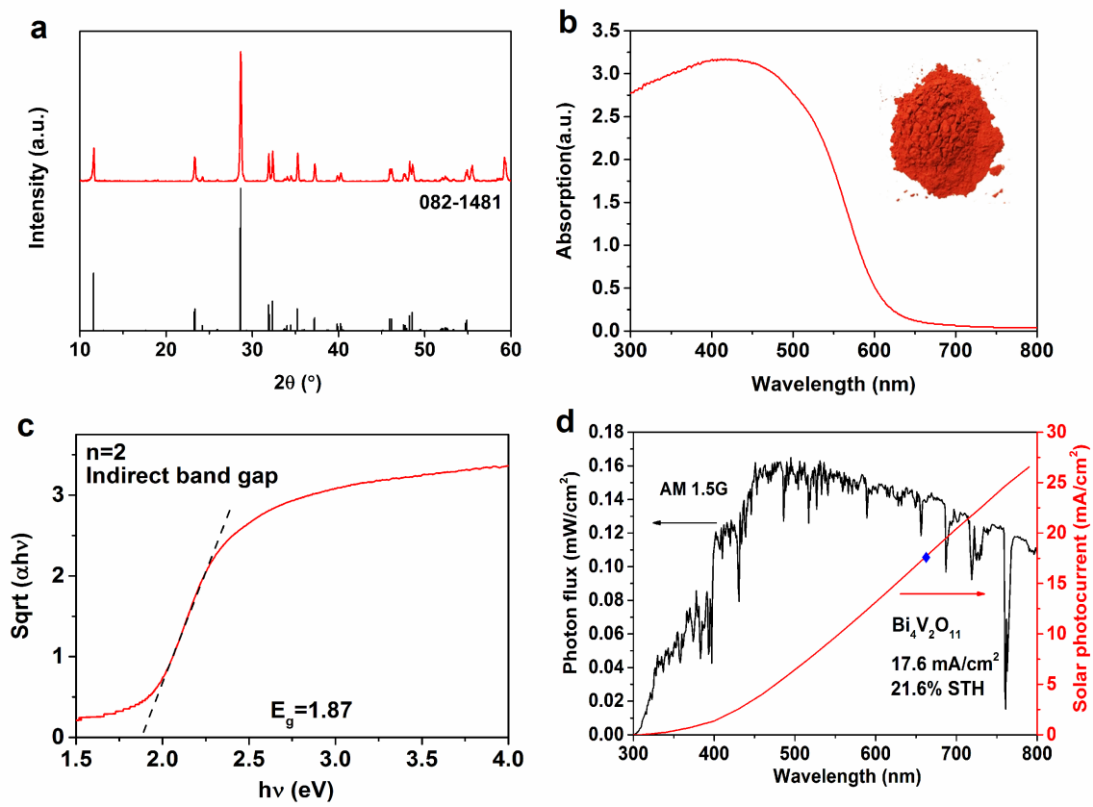

Figure 2. (**a**) X-ray diffraction of as synthesized $Bi_4V_2O_{11}$ powder by solid state reaction; (**b**) UV–vis light absorption spectrum of $Bi_4V_2O_{11}$ powder obtained from powder reflectance. Inset is the digital image of the synthesized powder; (**c**) Tauc plots of $Bi_4V_2O_{11}$ powder to estimate its bandgap; (**d**) Theoretical solar photocurrent density of $Bi_4V_2O_{11}$ under AM 1.5G irradiation (100 mW/cm^2).

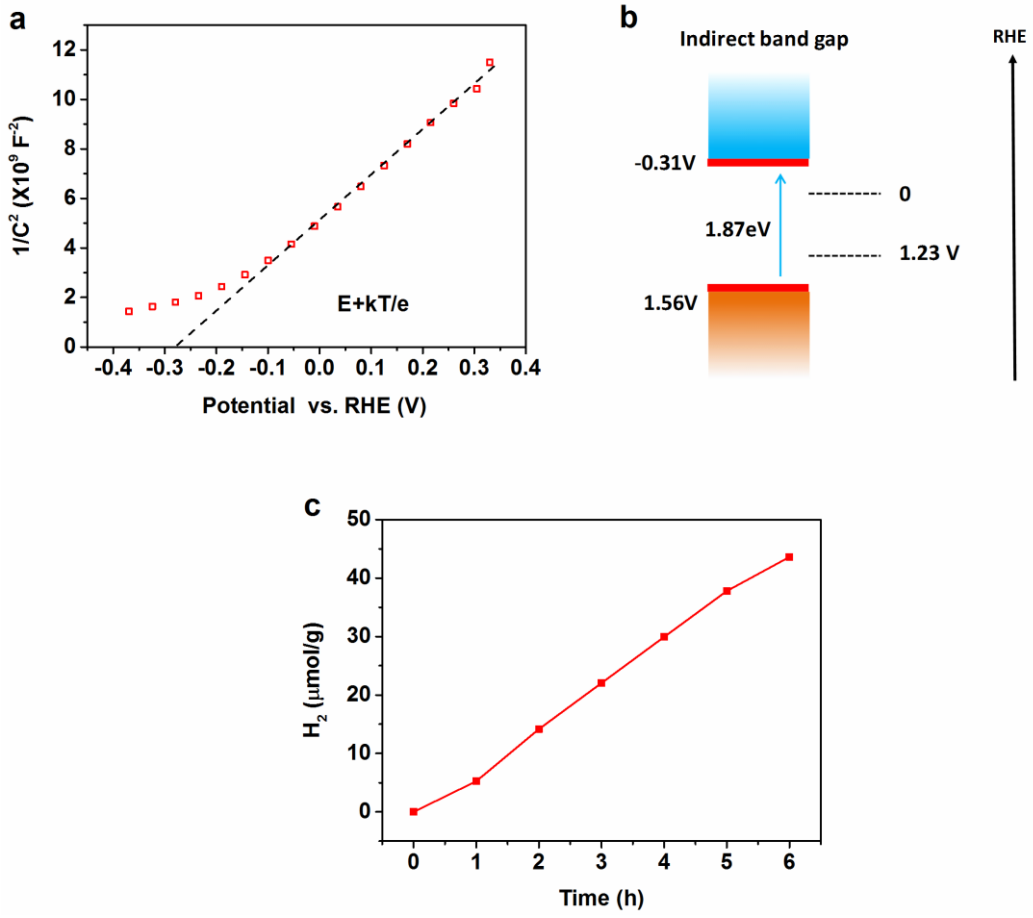

Figure 3. (**a**) Mott Schottky plot of $Bi_4V_2O_{11}$ film measured in 0.5 M Na_2SO_4 electrolyte under dark condition; (**b**) Diagram of the band position of $Bi_4V_2O_{11}$ compared with water redox potential; (**c**) Photocatalytic H_2 evolution of $Bi_4V_2O_{11}$ powder.

The PEC performance of pristine $Bi_4V_2O_{11}$ film was shown in Figure S2, which is very poor. Mo doping was employed to enhance the performance. Figure 4a shows SEM images of the Mo-doped $Bi_4V_2O_{11}$ film, which reveals that the particle size is about several microns. The crystal structure remains the same after Mo doping (Figure S3). Light absorption was almost the same with pure $Bi_4V_2O_{11}$ (Figure S4). Thus, Mo doping does not significantly change physical properties of $Bi_4V_2O_{11}$. Figure 4b shows the photocurrents of Mo-doped $Bi_4V_2O_{11}$ photoelectrodes, which is much higher than pure one without doping (Figure S2). This performance improvement is mainly benefited from the higher carrier density by Mo doping (Figure S5). It has been reported the particle connection was very important for the powder-fabricated thin films, and necking was necessary to improve the carrier transport between particles [9,10,31,33], since necking treatment can form effective contacts between the photocatalyst particles which facilitates the electron transport between the particles [34]. The one without necking treatment shows poor performance. Tungsten and titanium necking treatment were employed here. The photocurrent increases greatly with W necking compared with the one without, which reaches a maximum photocurrent of about 0.3 mA/cm^2. However, it was found that the Ti necking treatment shows even worse performance than the one without necking. To exclude WO_3 contribution to the photocurrent, the same amount of W necking agent was dropped on FTO substrate and followed by the same heating treatment as that of Mo-doped $Bi_4V_2O_{11}$ photoelectrode. The obtained WO_3 photoelectrode shows very weak photocurrent (Figure S6) with the maximum photocurrent less than 0.05 mA/cm^2. We also optimized the necking treatment temperature (Figure S7) and found that 500 °C shows the best performance. Different amount of catalysts was employed using powder suspension dropped on the FTO substrates (Figure S8), and the 2 mg/cm^2 sample shows the best performance. Figure 4c shows the wavelength dependence of the incident photon to current efficiency (IPCE) of Mo-doped $Bi_4V_2O_{11}$. The IPCE was calculated based on the measured constant potential I-t curves to avoid the transient photocurrent under monochromatic light irradiation. The IPCEs are consistent with I-V curves measured under simulated AM1.5G light, supporting the validity of the measurements. The stability of Mo-doped $Bi_4V_2O_{11}$ photoanode (active area about 2 cm^2) is tested under AM 1.5 G simulated sunlight condition (100 mW/cm^{-2}) at 1.23 V vs. RHE. After 2 h irradiation the photocurrent density drops to about 0.24 mA, which is around 80% of the initial value (around 0.3 mA). This is a reasonably good performance in photo stability without any surface protection. The primary reason for the current drop lies in the stability of the necking agent, since WO_3 is not stable in a neutral electrolyte solution. Some methods can be used to improve the stability such as coating a thin layer of protection oxides or changing the necking agent.

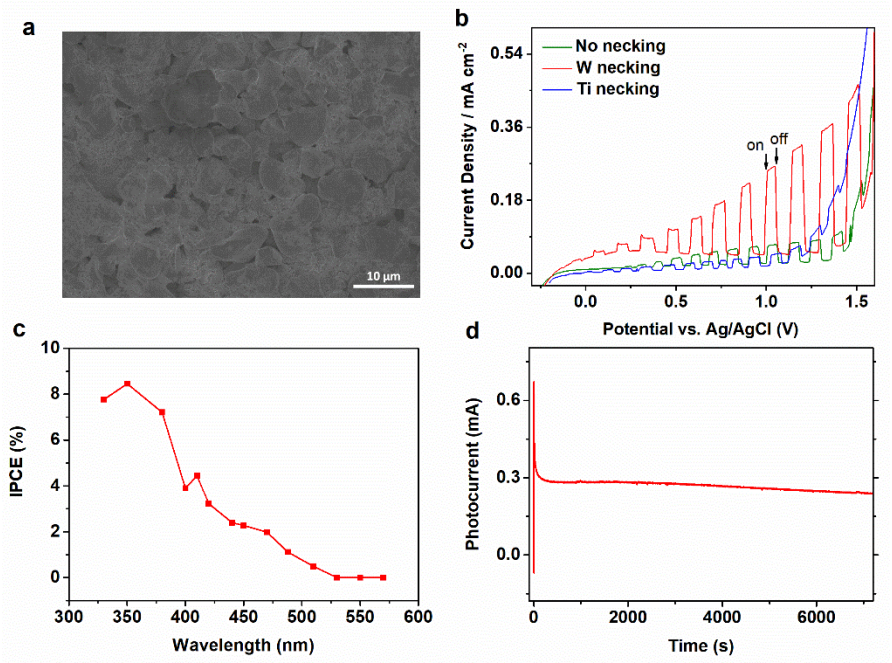

Figure 4. (**a**) SEM image of Mo-doped $Bi_4V_2O_{11}$ film prepared by drop-casting method; (**b**) Photocurrents (in chop mode with light on-off repeatedly) of Mo-doped $Bi_4V_2O_{11}$ photoelectrodes without the necking treatment and ones with W and Ti necking. Light on and off states were indicated; (**c**) IPCE of Mo-doped $Bi_4V_2O_{11}$ film at 1.23 V vs. RHE; (**d**) Stability test of Mo-doped $Bi_4V_2O_{11}$ film.

Discussion on the Limitation Factors of the Reported Performance

The water oxidation photocurrent J_{H_2O} can be expressed by [35]:

$$J_{H_2O} = J_0 \times \eta_{abs} \times \eta_{sep} \times \eta_{tran} = J_{abs} \times \eta_{sep} \times \eta_{tran} \quad (1)$$

where J_0 is the theoretical solar photocurrent density which assumes that all the solar energy corresponding to the band edge can be fully converted to fuel energy [36]. The charge transfer efficiency can be approximated to be 100% ($\eta_{inj} = 1$) when an effective hole scavenger Na_2SO_3 with fast oxidation kinetics is utilized [35]. The Na_2SO_3 oxidation photocurrent can be determined by [36]:

$$J_{Na_2SO_3} = J_0 \times \eta_{abs} \times \eta_{sep} = J_{abs} \times \eta_{sep} \quad (2)$$

where $J_{Na_2SO_3}$ is the oxidation photocurrent using Na_2SO_3. Combining Equations (1) and (2), we obtain the charge separation efficiency $\eta_{sep} = J_{Na_2SO_3}/J_{abs}$ and the charge transfer efficiency $\eta_{tran} = J_{H_2O}/J_{Na_2SO_3}$.

Figure 5a shows the light absorption efficiency of the as-fabricated film. The calculated J_{abs} by integrating the light absorption efficiency over the solar spectrum (AM 1.5 G) is estimated to be 7.6 mA/cm^2. Figure 5b,c shows the calculated charge separation efficiency, η_{sep}, and the charge transfer efficiency, η_{tran}, which are about 3% and 60% at 1.23 V vs. RHE, respectively. Thus, poor charge separation is the limitation factor, which results in the low photocurrent performance. The poor charge separation is mainly limited by the fabrication method through two aspects: (1) big particle size and the corresponding thick film have unnecessarily extended distance that the carriers have to travel, and thus increased the chance of recombination; (2) weak adhered boundaries between particles may have resulted in severe recombination. To improve the performance, more effort is needed to reduce the particle size by either exploring low temperature synthesis method for finer particles or making use vapor deposition method to prepare the film directly.

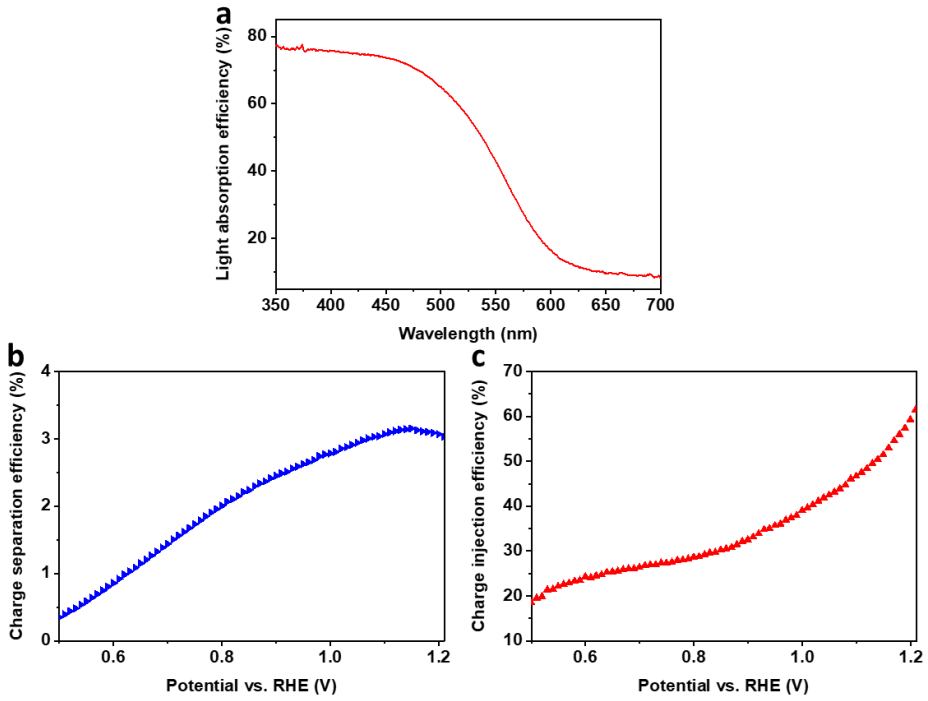

Figure 5. (**a**) Light absorption efficiency (**b**) charge separation efficiency and (**c**) charge transfer efficiency of Mo doped $Bi_4V_2O_{11}$ film.

4. Conclusions

$Bi_4V_2O_{11}$ possesses a red color with a bandgap of ~1.9 eV, corresponding to a highly promising solar to hydrogen efficiency. The CBM is more negative than water reduction potential of H^+/H_2 and VBM is more positive than the water oxidation potential of O_2/H_2O. This has made the material attractive for non-biased water splitting. Pristine $Bi_4V_2O_{11}$ films show quite poor performance, and Mo doping can greatly enhance the photocurrent by enhancing the charge carrier density. W necking was necessary to lead to a better performance in our case of films consisting of relatively large particles. The maximum photocurrent of Mo-doped $Bi_4V_2O_{11}$ photoanode reaches a value of about 0.3 mA/cm^2 with W necking treatment. The Mo-doped $Bi_4V_2O_{11}$ photoanode maintains 80% photocurrent after 2 h test, displaying reasonably good stability among known visible light active photocatalysts. The reason for the limited PEC performance has been analysed with potential strategies proposed to overcome the limitations for this promising photoanode material.

Supplementary Materials

The following supporting information can be found at: https://www.sciepublish.com/article/pii/167. DFT calculation method; Figure S1. SEM images of as synthesized $Bi_4V_2O_{11}$ particles; Figure S2. Photocurrent of pristine $Bi_4V_2O_{11}$ photoelectrode with W necking treatment; Figure S3. X-ray diffraction of Mo doped $Bi_4V_2O_{11}$ powder by solid state reaction; Figure S4. UV-vis light absorption spectrum of Mo doped $Bi_4V_2O_{11}$ powder; Figure S5. Mott Schottky plot of Mo doped $Bi_4V_2O_{11}$ film measured in 0.5 M Na_2SO_4 electrolyte under dark condition; Figure S6. Photocurrent of WO_3 obtained by dropping the same amount as necking agent on FTO substrate and heated at 500 ℃ for 1 h; Figure S7. Photocurrent of W necking samples treated with different temperature; Figure S8. Photocurrent of samples with different amount of powder suspension dropped on the FTO substrates.

Author Contributions

Conceptualization, J.H., J.F., and Z.C.; Methodology, X.Z. and J.F.; Validation, X.Z., J.H., J.F.; Formal Analysis, X.Z. and Y.Y.; Investigation, X.Z., N.Z., T.F. and J.F.; Resources, Z.C. and J.F.; Data Curation, J.H. and J.F.; Writing—Original Draft Preparation, Z.X. and Y.Y.; Writing—Review & Editing, Z.C.; Supervision, J.H., J.F. and Z.C.; Project Administration, Z.C.; Funding Acquisition, Z.C.

Ethics Statement

Not applicable.

Informed Consent Statement

Not applicable.

Funding

This research was funded by the National Research Foundation, Singapore for funding through a CREATE Program.

Declaration of Competing Interest

The authors declare that they have no known competing financial interests or personal relationships that could have appeared to influence the work reported in this paper.

References

1. Wang Z, Wu Q, Wang J, Yu Y. Surface modification by ligand growth strategy for dense copper bismuth film as photocathode to enhance hydrogen production activity. *Front. Energy* **2023**, doi:10.1007/s11708-023-0893-5.
2. Jun SE, Kim Y-H, Kim J, Cheon WS, Choi S, Yang J, et al. Atomically dispersed iridium catalysts on silicon photoanode for efficient photoelectrochemical water splitting. *Nat. Commun.* **2023**, *14*, 609.
3. Wang X, Gong J, Dong Y, An S, Zhang X, Tian J. Energy band engineering of hydroxyethyl group grafted on the edge of 3D g-C_3N_4 nanotubes for enhanced photocatalytic H_2 production. *Mater. Today Phys.* **2022**, *27*, 100806.
4. Díez-García MI, Gómez R. Progress in ternary metal oxides as photocathodes for water splitting cells: optimization strategies. *Sol. RRL* **2022**, *6*, 2100871.
5. Hitoki G, Ishikawa A, Takata T, Kondo JN, Hara M, Domen K. Ta_3N_5 as a novel visible light-driven photocatalyst ($\lambda < 600$ nm). *Chem. Lett.* **2002**, *31*, 736–737.
6. Kawase Y, Higashi T, Obata K, Sasaki Y, Katayama M, Domen K, et al. Interfacial design of a Ta_3N_5 thin-film photoanode for highly stable oxygen evolution over a wide pH range. *ACS Sustain. Chem. Eng.* **2022**, *10*, 14705–14714.
7. Hara M, Hitoki G, Takata T, Kondo JN, Kobayashi H, Domen K. TaON and Ta_3N_5 as new visible light driven photocatalysts. *Catal. Today* **2003**, *78*, 555–560.
8. Minegishi T, Nishimura N, Kubota J, Domen K. Photoelectrochemical properties of $LaTiO_2N$ electrodes prepared by particle transfer for sunlight-driven water splitting. *Chem. Sci.* **2013**, *4*, 1120–1124.
9. Feng J, Luo W, Fang T, Lv H, Wang Z, Gao J, et al. Highly photo-responsive $LaTiO_2N$ photoanodes by improvement of charge carrier transport among film particles. *Adv. Funct. Mater.* **2014**, *24*, 3535–3542.
10. Zhong Y, Li Z, Zhao X, Fang T, Huang H, Qian Q, et al. Enhanced water-splitting performance of perovskite $SrTaO_2N$ photoanode film through ameliorating interparticle charge transport. *Adv. Funct. Mater.* **2016**, *26*, 7156–7163.
11. Kim Y-I, Si W, Woodward PM, Sutter E, Park S, Vogt T. Epitaxial thin-film deposition and dielectric properties of the perovskite oxynitride $BaTaO_2N$. *Chem. Mater.* **2007**, *19*, 618–623.

12. Li Z, Luo W, Zhang M, Feng J, Zou Z. Photoelectrochemical cells for solar hydrogen production: Current state of promising photoelectrodes, methods to improve their properties, and outlook. *Energy Environ. Sci.* **2013**, *6*, 347–370.
13. Luo W, Yang Z, Li Z, Zhang J, Liu J, Zhao Z, et al. Solar hydrogen generation from seawater with a modified $BiVO_4$ photoanode. *Energy Environ. Sci.* **2011**, *4*, 4046–4051.
14. Alexander BD, Kulesza PJ, Rutkowska I, Solarska R, Augustynski J. Metal oxide photoanodes for solar hydrogen production. *J. Mater. Chem.* **2008**, *18*, 2298–2303.
15. Fujishima A, Honda K. Electrochemical photolysis of water at a semiconductor electrode. *Nature* **1972**, *238*, 37–38.
16. Cho IS, Han HS, Logar M, Park J, Zheng X. Enhancing low-bias performance of hematite photoanodes for solar water splitting by simultaneous reduction of bulk, interface, and surface recombination pathways. *Adv. Energy Mater.* **2016**, *6*, 1501840.
17. Piekner Y, Ellis DS, Grave DA, Tsyganok A, Rothschild A. Wasted photons: Photogeneration yield and charge carrier collection efficiency of hematite photoanodes for photoelectrochemical water splitting. *Energy Environ. Sci.* **2021**, *14*, 4584–4598.
18. Chen X, Liu J, Wang H, Ding Y, Sun Y, Yan H. One-step approach to novel $Bi_4V_2O_{11}$ hierarchical hollow microspheres with high visible-light-driven photocatalytic activities. *J. Mater. Chem. A* **2013**, *1*, 877–883.
19. Kumar S, Sahare PD. Photocatalytic activity of bismuth vanadate for the degradation of organic compounds. *Nano* **2013**, *08*, 1350007.
20. Lv C, Chen G, Sun J, Zhou Y. Construction of α–β phase junction on $Bi_4V_2O_{11}$ via electrospinning retardation effect and its promoted photocatalytic performance. *Inorg. Chem.* **2016**, *55*, 4782–4789.
21. Ri C-N, Song-Gol K, Ju-Yong J, Pak S-N, Ri S-C, Ri J-H. Construction of the $Bi_2WO_6/Bi_4V_2O_{11}$ heterojunction for highly efficient visible-light-driven photocatalytic reduction of Cr(vi). *New J. Chem.* **2018**, *42*, 647–653.
22. Wen X-J, Qian L, Lv X-X, Sun J, Guo J, Fei Z-H, et al. Photocatalytic degradation of sulfamethazine using a direct Z-Scheme $AgI/Bi_4V_2O_{11}$ photocatalyst: Mineralization activity, degradation pathways and promoted charge separation mechanism. *J. Hazard. Mater.* **2020**, *385*, 121508.
23. Li J, Lu P, Deng W, Zeng Z, Lin L, Zhao G. Facile synthesis of sheet-like $BiVO_4/Bi_4V_2O_{11}$ composite for enhanced photocatalytic properties. *Mater. Chem. Phys.* **2020**, *254*, 123489.
24. Lin Y, Cai H, Chen H, Luo H. One-pot synthesis of $Bi_4V_2O_{11}/BiVO_4$ heterostructure with enhanced photocatalytic activity for dye degradation. *Appl. Surf. Sci.* **2021**, *544*, 148921.
25. dos Santos WS, Rodriguez M, Afonso AS, Mesquita JP, Nascimento LL, Patrocínio AOT, et al. A hole inversion layer at the $BiVO_4/Bi_4V_2O_{11}$ interface produces a high tunable photovoltage for water splitting. *Sci. Rep.* **2016**, *6*, 31406.
26. dos Santos WS, Rodriguez M, Khoury JMO, Nascimento LA, Ribeiro RJP, Mesquita JP, et al. Bismuth vanadate photoelectrodes with high photovoltage as photoanode and photocathode in photoelectrochemical cells for water splitting. *ChemSusChem* **2018**, *11*, 589–597.
27. Zhao X, Duan Z, Chen L. Bi-quantum-dot-decorated $Bi_4V_2O_{11}$ hollow nanocakes: Synthesis, characterization, and application as photocatalysts for CO_2 reduction. *Ind. Eng. Chem. Res.* **2019**, *58*, 10402–10409.
28. Liu J, Ozawa K, Uezono N, Pawar SA, Suzuki S, Traoré A, et al. Electronic structure of orthorhombic $Bi_4V_2O_{11}$ and role of gap states in photoelectrochemical water splitting. *J. Chem. Phys. C* **2023**, *127*, 11195–11203.
29. Wang Y, Liang S, Zuo C, Fang H, Dong G, Sheng X, et al. Construction of a heterojunction with fast charge transport channels for photocatalytic hydrogen evolution via a synergistic strategy of Co-doping and crystal plane modulation. *Nanoscale* **2023**, *15*, 5230–5240.
30. Wang Z, Zhang W, Song Y, Liu N, Chen L, An N, et al. Unraveling the site-selective doping mechanism in single-crystalline $BiVO_4$ thin films for photoelectrochemical water splitting. *J. Chem. Phys. C* **2023**, *127*, 5775–5782.
31. Feng J, Zhao X, Ma SSK, Wang D, Chen Z, Huang Y. Fast and simple construction of efficient solar-water-splitting electrodes with micrometer-sized light-absorbing precursor particles. *Adv. Mater. Technol.* **2016**, *1*, 1600119.
32. Sayama K, Nomura A, Arai T, Sugita T, Abe R, Yanagida M, et al. Photoelectrochemical decomposition of water into H_2 and O_2 on porous $BiVO_4$ thin-film electrodes under visible light and significant effect of Ag ion treatment. *J. Phys. Chem. B*, **2006**, *110*, 11352–11360.
33. Zhang L, Song Y, Feng J, Fang T, Zhong Y, Li Z, et al. Photoelectrochemical water oxidation of $LaTaON_2$ under visible-light irradiation. *Int. J. Hydrogen Energy*, **2014**, *39*, 7697–7704.
34. Higashi M, Domen K, Abe R. Fabrication of efficient TaON and Ta_3N_5 photoanodes for water splitting under visible light irradiation. *Energy Environ. Sci.* **2011**, *4*, 4138–4147.
35. Dotan H, Sivula K, Grätzel M, Rothschild A, Warren SC. Probing the photoelectrochemical properties of hematite (α-Fe_2O_3) electrodes using hydrogen peroxide as a hole scavenger. *Energy Environ. Sci.* **2011**, *4*, 958–964.
36. Zhao X, Luo W, Feng J, Li M, Li Z, Yu T, et al. Quantitative analysis and visualized evidence for high charge separation efficiency in a solid-liquid bulk heterojunction. *Adv. Energy Mater.* **2014**, *4*, 1301785.